Available online at www.sciencedirect.com
ScienceDirect
Trans. Nonferrous Met. Soc. China 33(2023) 2379−2394
Transactions of Nonferrous Metals Society of China
www.tnmsc.cn

Effect of gas pressure on microstructure and mechanical properties of TC11 titanium alloy during supersonic fine particle bombardment

Yong-li WU[1], Yi XIONG[1,2], Zheng-ge CHEN[3], Wei LIU[1,2], Xin ZHANG[1], Shu-bo WANG[4], Wei CAO[4]

1. School of Materials Science and Engineering, Henan University of Science and Technology, Luoyang 471023, China;
2. Provincial and Ministerial Co-construction Collaborative Innovation Center for Non-ferrous Metal New Materials and Advanced Processing Technology, Luoyang 471023, China;
3. State Key Laboratory of Laser Interaction with Matter, Northwest Institute of Nuclear Technology, Xi'an 710024, China;
4. Nano and Molecular Systems Research Unit, University of Oulu, FIN-90014, Finland

Received 28 February 2022; accepted 28 April 2022

Abstract: The surface nanocrystallization of a Ti−6.5Al−3.5Mo−1.5Zr−0.3Si (TC11) titanium alloy with a lamellar microstructure was carried out by supersonic fine particle bombardment (SFPB). The effect of SFPB gas pressure on its surface integrity, microstructural evolution and mechanical properties was systematically investigated. The results showed that gradient nanostructures on the surface of the TC11 alloy were successfully created after SFPB with different gas pressures. The grain size of the surface's lamellar microstructure was completely refined to the nanometer scale. And the grain size of nanocrystals decreased with the increase of gas pressure. Meanwhile, the subsurface retained initial lamellar microstructure morphology. Surface roughness was minimized after SFPB with a gas pressure of 1.0 MPa, while microcrack formed at a higher gas pressure of 1.5 MPa, resulting in a decrease of compressive residual stress. With the increase of SFPB gas pressure, the surface microhardness and the depth of hardened layer gradually increased, and yield strength and tensile strength was improved. Nevertheless, the elongation was not greatly changed. The fracture morphology changed from typical ductile fracture to quasi-cleavage and ductile mixed fracture.
Key words: supersonic fine particle bombardment; gas pressure; titanium alloy; lamellar microstructure; surface nanocrystallization; microstructure; mechanical properties

1 Introduction

Ti alloys are widely used in the aerospace, marine, petrochemical and chemical industries because of their high specific strength, excellent fatigue properties and corrosion resistance [1−3]. However, their service life decreases sharply in harsh and complex environments. To improve their service life and to avoid premature failure in the form of fatigue fracture, frictional wear and corrosion, principally caused by surface damage [4], it is essential to investigate efficient surface strengthening methods to alter the surface properties and thus to enhance the service performance of Ti alloy components. For example, surface nanocrystallization achieved via various techniques is a novel, easy-to-operate and non-polluting surface strengthening technique [5]. Gradient surface nanostructures of Ti alloy components, prepared by using surface nano-crystallization techniques, e.g. surface mechanical attrition treatment (SMAT) [6], ultrasonic impact treatment (UIT) [7], and ultrasonic and laser shot peening (USP and LSP) [8,9], can improve mechanical properties [7], fatigue properties [10]

Corresponding author: Yi XIONG, Tel: +86-13526917962, E-mail: xiongy@haust.edu.cn
DOI: 10.1016/S1003-6326(23)66266-1

and corrosion resistance [11] of the components.

Supersonic fine particle bombardment (SFPB) is a more advanced and efficient shot peening impact technique of surface nanocrystallization developed from traditional shot peening [12]. Compared with SMAT, UIT, USP and other techniques, SFPB is versatile and is able to treat components of different sizes and those with especially complex shapes and large flat surfaces. Furthermore, the equipment is not as expensive as LSP equipment, and thus it is also more economical for industrial applications [13].

Currently, SFPB has been successfully applied to various metallic materials and can enhance the overall properties of components [14−17]. ZHANG et al [18] found that the textured nanocrystals formed on a pure Ti surface by SFPB could significantly improve the alloy's wear resistance. GE et al [19,20] used SFPB to prepare randomly oriented equiaxed grains with a size of about 20 nm on the surface of pure Ti samples. The nanocrystals obtained were thermally stable and played a critical role in the enhancement of creep strength. ZHAO et al [21] produced nanostructures on the surface of a TC17 alloy with the aid of SFPB. It was noted that the nanostructure's layer thickness increased with increasing SFPB treatment time, and the grain size was gradually refined to about 16.3 nm and stabilized after 30 min of treatment. Our previous work [22] showed that the TC11 alloy achieved surface nanocrystallization after SFPB, thus resulting in a momentous increase in the fatigue strength of TC11 alloys. From the above research background, it can be seen that the application of SFPB technology can realize the surface nano-crystallization of Ti and its alloy components, which can dramatically improve the service performance of their components. However, most of its research objects are mainly based on equiaxed microstructure, while the association between the SFPB technological parameters and mechanical properties of Ti alloy has not been addressed.

TC11 alloys with a lamellar microstructure have better fracture toughness, higher crack propagation resistance and better durability and creep strength than alloys with an equiaxed microstructure [23]. Nevertheless, such lamellar microstructures are more sensitive to surface defects, and thus surface modification is required. In this work, a gradient nanostructure was prepared by SFPB on the surface of TC11 alloys with an initial lamellar microstructure. The influence of SFPB gas pressure on the surface integrity, microstructural evolution and mechanical properties of a TC11 alloy was systematically investigated, aiming to provide technical support for the application of SFPB technology in the industrial field of Ti alloys.

2 Experimental

2.1 Materials

The nominal chemical composition of the TC11 alloy was 6.5 Al, 3.5 Mo, 1.5 Zr and 0.3 Si (wt.%), and balanced Ti. The phase transformation temperature of TC11 alloy was determined to be 970 ℃ by metallographic method. The initial lamellar microstructure was achieved by forging slab-shaped TC11 alloys with dimensions of 14 mm × 18 mm × 150 mm and by duplex annealing using an Ar gas-protected vacuum furnace. The duplex annealing was performed as follows: firstly, the material was heated to 970 ℃ and held for 1.5 h, followed by air-cooling to room temperature, then reheating to 530 ℃ and holding for 6 h; finally, the alloy was air-cooled to room temperature. The obtained lamellar microstructure is shown in Fig. 1.

2.2 Methods

The duplex-annealed TC11 alloy was machined by wire cutting into sheet-like tensile samples, as shown in Fig. 2. Prior to SFPB, these tensile samples were mechanically ground, polished and cleaned. SFPB, for which a schematic illustration is shown in Fig. 3 [14], was conducted in the black shaded surface area in Fig. 2 on both sides for 60 s with a gas pressure of 0.5, 1.0 and 1.5 MPa, respectively. In our study, after 1.0 MPa for more than 60 s, microcracks formed on the surface, leading to a decrease in tensile properties, so 60 s was chosen to research the effect of different gas pressures on the properties of TC11 alloy. The details of the SFPB processing parameters were as follows: the bombardment temperature was room temperature, the carrier gas was air, the projectile injection distance was 30 mm, the projectile injection angle was 90°, and the bombardment particles were chosen to be spherical Al_2O_3 particles with an average size of 50 μm, as reported in Ref. [22].

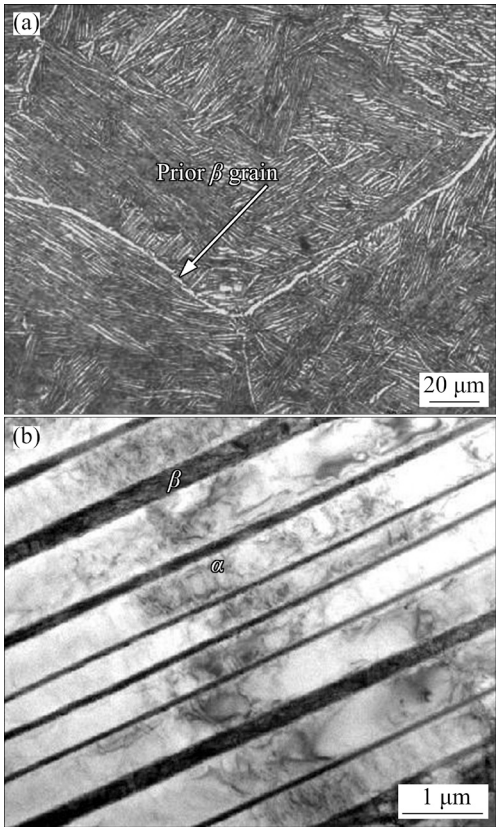

Fig. 1 OM (a) and TEM (b) images of duplex-annealed TC11 alloy with lamellar microstructure

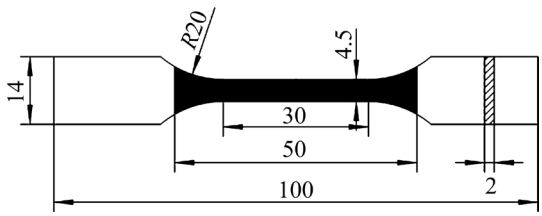

Fig. 2 Schematic drawing of dimensions of tensile sample (The black shaded area represents the SFPB-treated area on both sides of the tensile samples) (unit: mm)

The surface roughness of the SFPB-treated samples was measured with a Nanovea HS1000P 3D surface topographer. The corresponding surface morphologies were observed with a JSM−IT200 scanning electron microscope (SEM). The X-ray diffractometry (XRD) patterns of SFPB-treated samples with different gas pressures were obtained by a D8 ADVANCE X-ray diffractometer with a Cu target. The scan step and scan range were set to be 0.02° and 30°−80°, respectively. The cross-sections of the samples in different states (perpendicular to the surface treatment direction) were ground, polished, etched with hydrofluoric acid, nitric acid (HNO_3) and clean water (H_2O) solutions with a volume ratio of 5:12:83, and cleaned before the observation of the microstructure morphology with a JSM−7800F SEM. Thin specimens of a 0.5 mm thickness were sliced from the sections of the samples on surface and subsurface. These thin slices were mechanically ground to a thickness of about 50 μm, from which *d*3 mm discs were punched at different locations. Final *d*3 mm thin foils were prepared by double-spray electrolytic polishing using a 6% $HClO_4$ + 34% C_4H_9OH + 60% CH_3OH (volume fraction) electrolyte at −30 °C (cooled down by liquid nitrogen). The thinning voltage and current were 14 V and 60−80 mA, respectively. The microstructure of surface and subsurface (100 μm from the surface) was observed using a JEM−2010 TEM operated at 200 kV. Using the electrolytic polishing method, the residual stresses at different layer depths of the samples processed by different SFPB gas pressures were measured by an X−350A X-ray stress analyzer. The center of the SFPB-treated area of each layer was selected for the

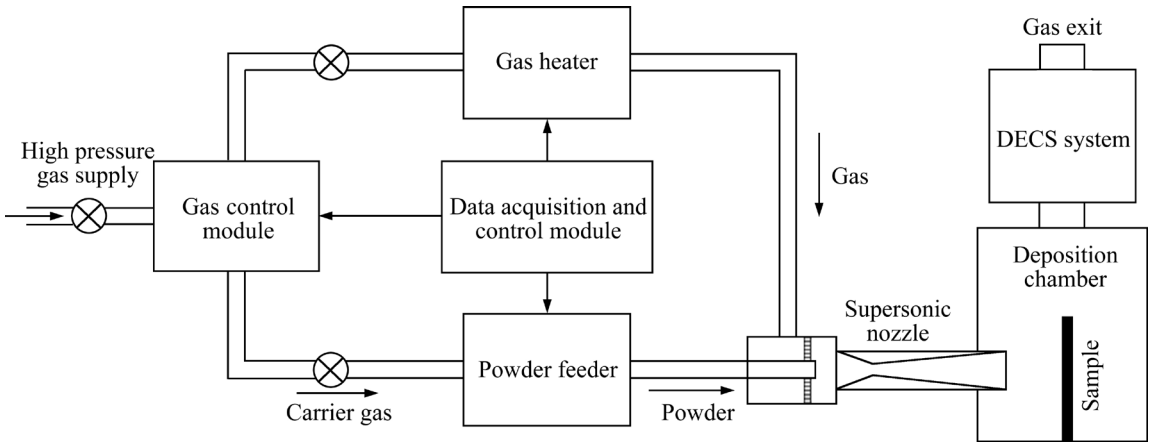

Fig. 3 Schematic illustration of SFPB treatment [14]

measurements. The final value at the depth of the layer was an average of at least three measurements obtained with a Cu K_α X-ray source at the (213) crystal planes of the α-phase. The voltage and current were 27 kV and 7 mA, respectively. The tube's diameter was 4 mm, and the heeling angle was selected as 0°, 15°, 30° or 45°, respectively. The microhardness of the longitudinal section of the samples in different states was measured with an MH−3 microhardness tester, and the loading force and dwelling time were set to be 0.98 N and 10 s, respectively. To ensure the accuracy of measurement results, five different locations were selected for each depth, then the average value was taken as the final microhardness value. The mechanical properties of the SFPB-treated samples were tested on an INSTRON 5587 tensile testing machine with at least three measurements at room temperature, a loading speed of 0.5 mm/min, and a tensile strain rate of 0.1 mm/s. The fracture morphology was observed with a JSM−7800F SEM.

3 Results and discussion

3.1 Surface integrity

Figure 4 shows SEM images of the surface morphologies and 3D topography of the TC11 alloy after SFPB with different gas pressures. The surface of the TC11 alloy before SFPB is relatively smooth: only evenly distributed scratches from mechanical grinding and polishing exist (Fig. 4(a)). Correspondingly, the surface roughness (S_a) and surface peak-to-valley height (H_{PV}) calculated by 3D topography are small: 0.564 and 4.835 μm, respectively (Fig. 4(b)). The surface morphology is changed by SFPB with different gas pressures, as evidenced by the significantly increased S_a and H_{PV}. At 0.5 MPa (Fig. 4(c)), there are multiple microdents and honeycomb impact pits caused by the bombardment of Al_2O_3 particles with high energy and high speed on the sample surface. In addition, the metal material around microdents undergoes flow plastic deformation, and accumulation occurs at the boundary of microdents, forming "peaks" and "valleys" [24], making the surface become much rougher with S_a and H_{PV} values of 8.546 and 121.950 μm, respectively (Fig. 4(d)). When the gas pressure increases to 1.0 MPa, the surface of the sample becomes relatively flat and honeycomb impact pits depth becomes shallow (Fig. 4(e)), showing S_a and H_{PV} values of 6.186 and 100.481 μm, respectively (Fig. 4(f)). At 1.5 MPa, "peaks" and "valleys" form again, and small impact pits are visible (Fig. 4(g)). Long cracks inside the microdents are also noticeable (Fig. 4(g)). The surface is significantly rougher, with S_a of 9.146 μm and H_{PV} of 135.256 μm (Fig. 4(h)), larger than those SFPB-treated at 1.0 MPa.

The impact velocity of the Al_2O_3 particles and the impact kinetic energy increase with increasing gas pressure [25], thereby making the degree of plastic deformation occurring on the surface increase. With increasing SFPB time, the surface morphological features, which form in a shorter time, could fade because of the continuous deformation by the ongoing impact of high-energy Al_2O_3 particles. At 1.0 MPa, the impact velocity of Al_2O_3 particles and the impact kinetic energy increase compared with those at 0.5 MPa. Consequently, the degree of plastic deformation increases, and the accumulations formed at the shorter impact time fade. Therefore, the sample surface at 1.0 MPa with an impact time of 60 s is relatively flat and the surface roughness is reduced, as compared to those at 0.5 MPa. At a higher gas pressure, e.g., 1.5 MPa, the sample surface could be relatively flat before reaching 60 s of SFPB processing time. In this case, clear accumulations reappear on the relatively flat area when the impact time increases to 60 s, resulting in a significant increase in surface roughness compared to that at 1.0 MPa. Additionally, according to the elastic-plastic deformation theory and plastic hardening characteristics, subsequent or severer impacts can only cause slight plastic deformation in the initial work-hardened surface area [14], leading to the formation of small impact pits connected in rows at the bottom of the microdent (Fig. 4(g)). Meanwhile, because of uncoordinated plastic deformation of the α- and β-phases of two-phase Ti alloys [26], initiation and propagation of microcracks appear at the stress concentration point. Therefore, the selection of a suitable SFPB gas pressure and the associated impact time (60 s) is important for the surface integrity of the sample. Excessive roughness can result in stress concentration as well as defects on the surface of a component after the surface treatment, which

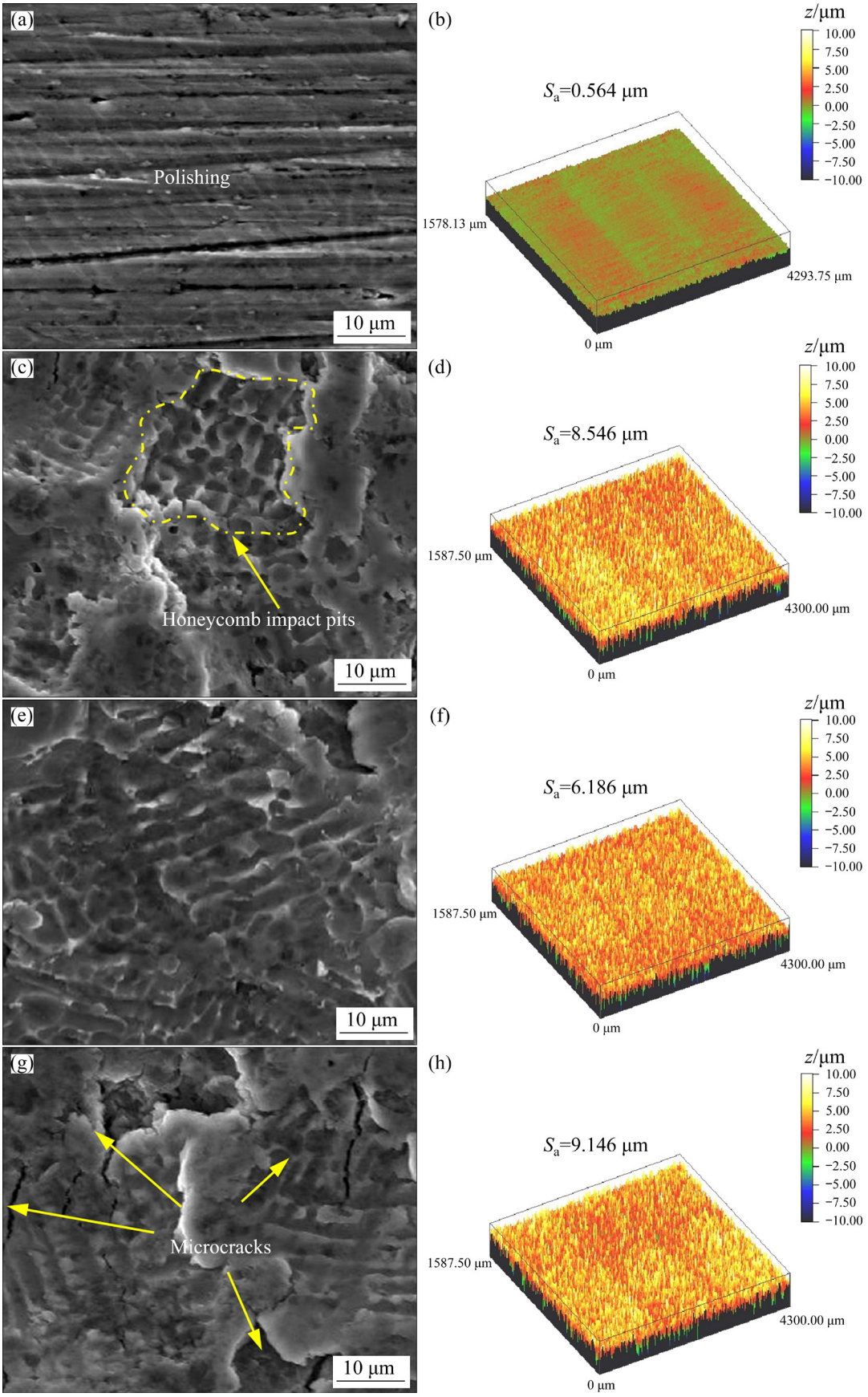

Fig. 4 2D and 3D surface morphologies of TC11 alloy after SFPB with different gas pressures: (a, b) Untreated; (c, d) 0.5 MPa for 60 s; (e, f) 1.0 MPa for 60 s; (g, h) 1.5 MPa for 60 s

subsequently reduces the service life of the component [27].

3.2 Microstructural evolution

3.2.1 Cross-sectional SEM observations

Figure 5 displays the cross-section SEM images of TC11 alloys, in which the brighter areas represent the β-phase while darker areas represent α-phase. A typical lamellar microstructure has been obtained after duplex annealing (Fig. 5(a)). After SFPB at 0.5 MPa, the surface microstructure of the TC11 alloy is severely plastic deformed by SFPB, as evidenced by the facts that the prior straight lamellar microstructure is either parallel or perpendicular to the surface before bombardment bend, the β-lamellae spacing is reduced and the prior grain boundaries become less distinguishable (Fig. 5(b)). The microstructures formed under the adjacent impact microdents are kinked and bent at the intersections because of the different degrees of deformation (Fig. 5(b)). The deformation layer on the surface of the TC11 alloy with a lot of bends and kinks and the β-lamellae with reduced spacing is defined as the SPD layer. This layer is found to have a thickness of about 29 μm at 0.5 MPa. With the increase of gas pressure (Figs. 5(c, d)), the initial lamellar microstructure undergoes severer deformation, showing severer kinked deformation other than bending, and even fracture due to severe kinks. A smaller β-lamellae spacing far from the surface can also be found at 1.5 MPa (Fig. 5(d)). The thickness of the SPD layer increases to be about 50 μm at 1.0 MPa and 63 μm at 1.5 MPa.

As we know from the above, the closer the distance to the surface is, the severer the plastic deformation is. As the distance from the topmost surface increases, the degree of deformation decreases, and the β-lamellae spacing gradually increases and then remains the same as the matrix value, which is related to the decay of energy during SFPB. In addition, as the SFPB gas pressure increases, the internal stresses converted from the kinetic energy of Al_2O_3 bombardment particle increase, the degree of plastic deformation on the surface of the TC11 alloy becomes severer, and the SPD layer becomes deeper.

3.2.2 XRD patterns

The duplex-annealed TC11 alloy consists of two phases: the α- and β-phases, as shown in Fig. 6(a). Broadened diffraction peaks are found

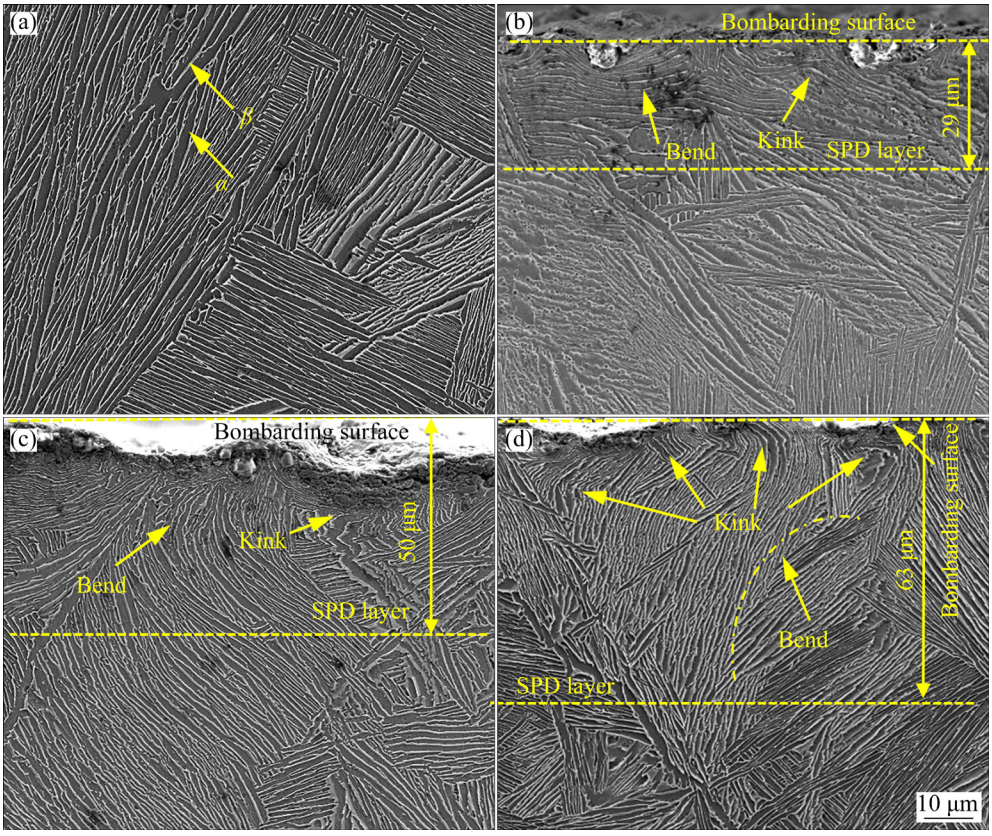

Fig. 5 Cross-sectional SEM images of TC11 alloy after SFPB with different gas pressures for 60 s: (a) Untreated; (b) 0.5 MPa; (c) 1.0 MPa; (d) 1.5 MPa

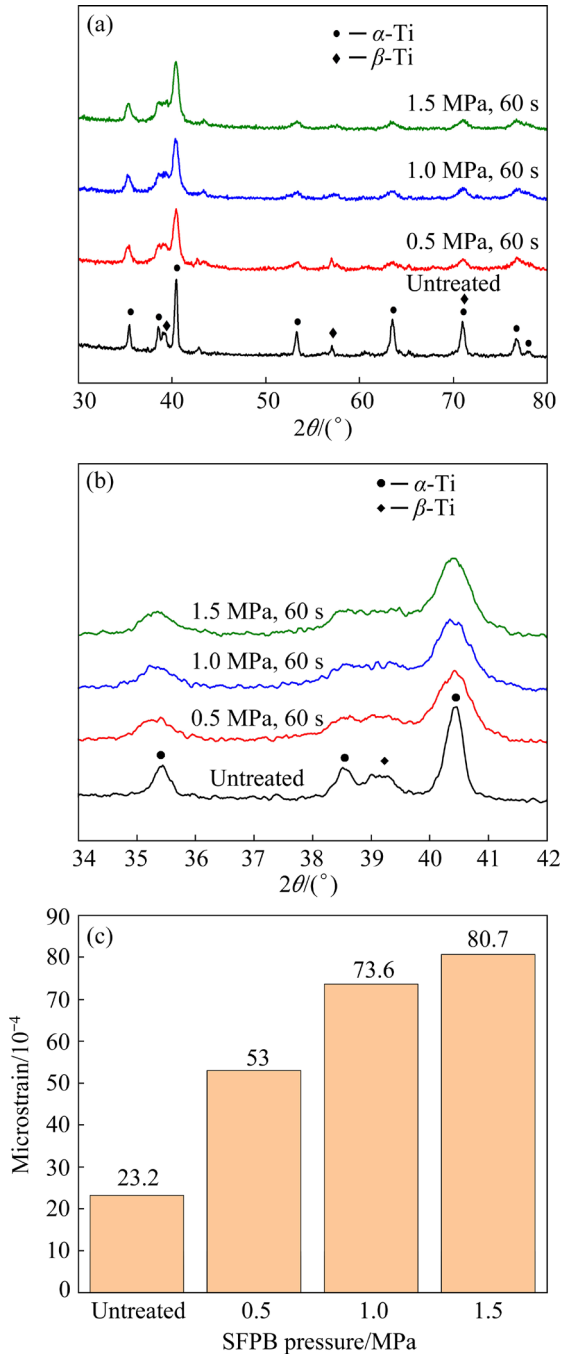

Fig. 6 XRD patterns and microstrain of TC11 alloy after SFPB with different gas pressures: (a) 30°−80° XRD patterns; (b) 34°−42° XRD patterns; (c) Calculated microstrain

in TC11 alloys after SFPB with different gas pressures. In the magnified view of XRD in Fig. 6(b), it is clear that the full width at half maximum (FWHM) of the diffraction peaks increases significantly after SFPB and gradually increases with an increase in the SFPB gas pressure. This is mainly caused by the increasing degree of SPD in the TC11 alloy after SFPB with different gas pressures (Fig. 5), resulting in the increase in the grain refinement and microstrain [28]. The microstrain can be evaluated according to the Williamson–Hall method [14]:

$$\beta\cos\theta=\varepsilon\left(4\sin\theta\right)+K\lambda/D \quad (1)$$

where β is the FWHM of the diffraction peak, K (≈0.9) is a constant, λ (=0.15406 nm) is the wavelength of X-ray, (Cu K_α source), D is the average grain size, θ is the Bragg diffraction angle, and ε is the microstrain. The microstrain of the surface in different states (Fig. 6(c)) is calculated to be 53×10^{-4}, 73.6×10^{-4} and 80.7×10^{-4} at 0.5, 1.0 and 1.5 MPa, which is 1.28, 2.17 and 2.48 times higher than the microstrain in the duplex-annealed state, respectively. In addition, the degree of surface grain refinement for different SFPB gas pressures is assessed using TEM.

3.2.3 TEM observations

Figure 7 shows the TEM images of the TC11 alloy's surface after SFPB with different gas pressures. After SFPB, the TC11 alloy's lamellar microstructure is fragmented and the grain boundaries could not easily be distinguished in the bright-field images in Figs. 7(a, c, e). Incompletely fragmented lamellar microstructures, shown by arrows, are observable locally at a SFPB gas pressure of 0.5 MPa (Fig. 7(a)). As the gas pressure increases, the fragmentation becomes more complete (Figs. 7(c, e)). The selected area electron diffraction pattern in Fig. 7(a) shows multiple arcs, indicating that the grain size of TC11 alloy reaches the nanometer level at 0.5 MPa. In contrast, the diffraction rings are more continuous at 1.0 and 1.5 MPa (insets of Figs. 7(c, e)), suggesting severer grain refinement with increasing gas pressure [29]. To further analyze the grain size distribution after SFPB with different gas pressures, the Nano Measurer software is used to count the grain sizes of multiple dark-field images by applying a division lines method. The histogram of the grain size distribution (inset of Fig. 7(b)) shows that the average grain size is estimated to 17.7 nm. The grain size decreases to about 11.8 and 9.4 nm at an increase in gas pressure to 1.0 and 1.5 MPa, respectively (insets of Figs. 7(d, f)).

The TEM images of the TC11 alloy's subsurface after SFPB with different gas pressures are given in Fig. 8. Dislocation walls formed in the direction of the α-lamellar thickness at a gas

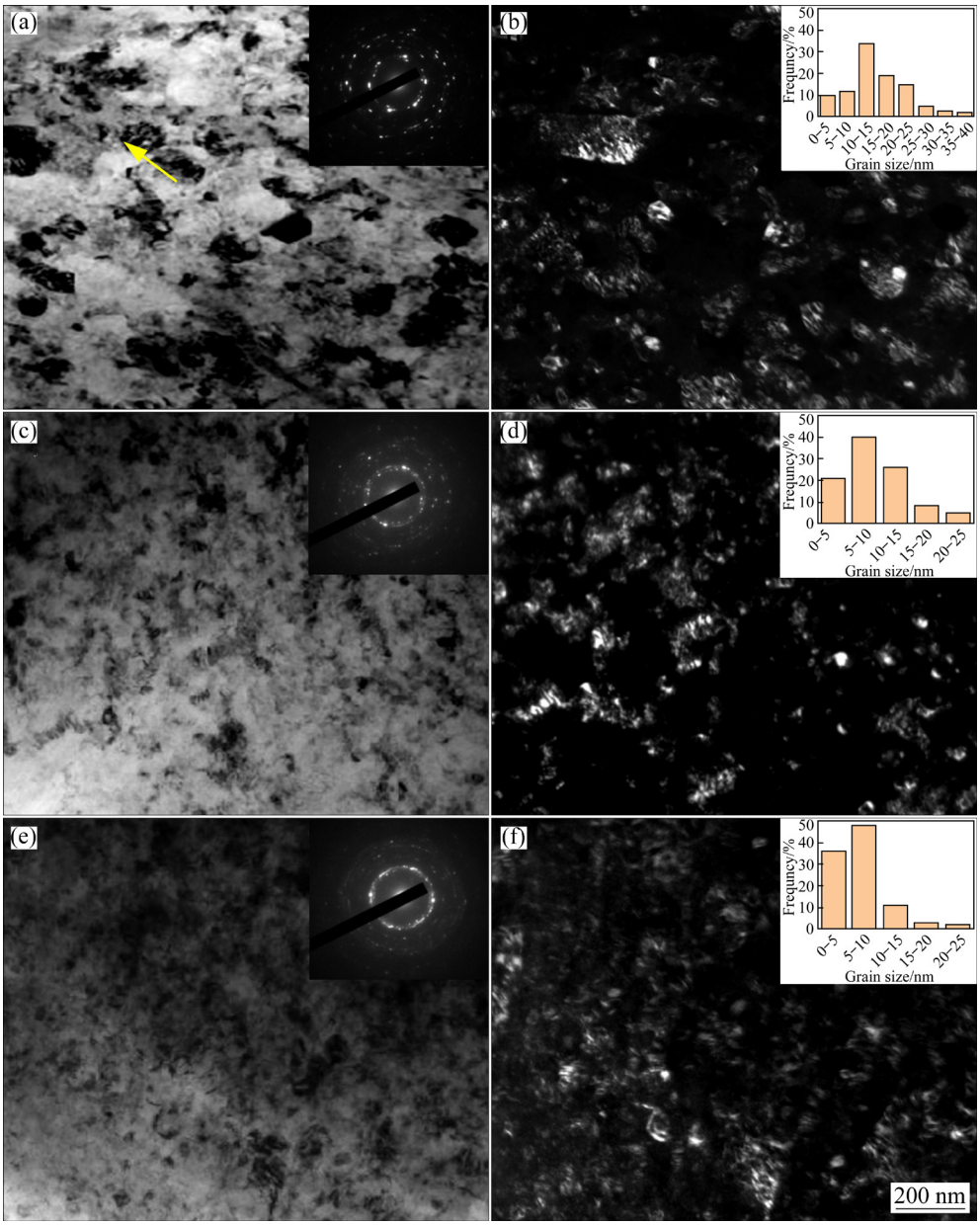

Fig. 7 TEM images of surface of TC11 alloy after SFPB with different gas pressures: (a, c, e) Bright-field images at 0.5, 1.0 and 1.5 MPa, respectively; (b, d, f) Corresponding dark-field images (The insets in (a, c, e) and (b, d, f) are selected area electron diffraction patterns and grain size distribution, respectively)

pressure of 0.5 MPa (Fig. 8(a)), indicating that dynamic recovery occurred and the dislocations were rearranged in a certain direction to form walls during the deformation process at this strain rate. Differences in the thickness and orientation of the dislocation walls can also be found, further suggesting that different slip systems were activated, i.e., besides the basal plane, prismatic and even pyramidal slip systems also came into play [30]. In addition, a high density of dislocation tangles can be observed at the α/β-phase boundary (Fig. 8(a)). Discrete dislocation lines also exist in the α-phase matrix (Fig. 8(b)), which could be ascribed to the neighboring dislocation walls that acted as a source of dislocation. As the gas pressure increased to 1.0 MPa (Figs. 8(c, d)), the degree of SPD increased, and the lamellar microstructure underwent bending and fracture (elliptical region) (Fig. 8(c)). The dislocation density within the α-lamellae increased significantly. When the gas pressure continued to increase up to 1.5 MPa (Figs. 8(e–h)), it could be observed that bending and fracture of the lamellar microstructure became severer (Fig. 8(e)). The dislocation tangles also

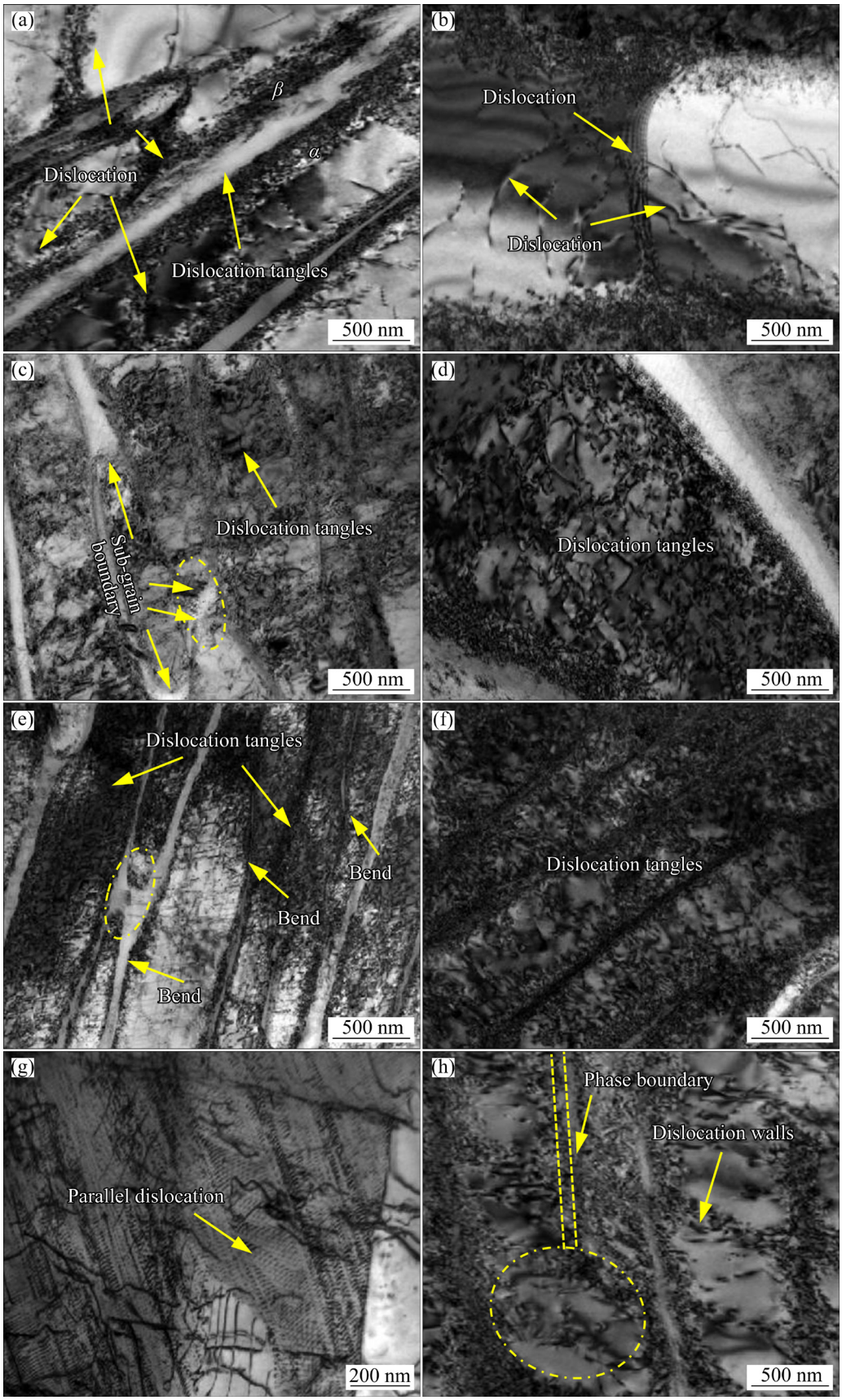

Fig. 8 TEM images of subsurface (100 μm from surface) of TC11 alloy after SFPB with different gas pressures: (a, b) 0.5 MPa for 60 s; (c, d) 1.0 MPa for 60 s; (e–h) 1.5 MPa for 60 s

became denser in Fig. 8(f), almost completely saturating the lamellar microstructure. Meanwhile, the dislocations were reorganized to form parallel-aligned dislocation structures in the α-lamellae to reduce the system's energy, which may continuously attract and emit dislocations and form dislocation bands or subgrain boundaries (Fig. 8(g)). It can also be observed from Fig. 8(h) that at 1.5 MPa more dislocation walls appear to split the α-lamellar microstructure into smaller regions, and it is worth noting that the dislocation walls in this state can split the α- and β-lamellae across the phase boundary, as shown in the elliptical region.

It can therefore be concluded that dislocation motion dominates the nanocrystallization process of the TC11 alloy after SFPB with different gas pressures, whereas deformation twinning is not seen. Similar phenomena have been found in Refs. [31,32]. During a SPD process with a high strain rate such as SFPB, the crystal structure and the stacking fault energy of metallic materials have an important influence on the surface nano-crystallization. The β- and α-phases in the dual-phase TC11 alloy have a body-centered cubic and a hexagonal close packed structure, respectively. The body-centered cubic metal has 12 slip systems, and the plastic deformation is dominated by dislocation motion. Whereas, for the hexagonal close packed metal, there are only four independent slip systems, so twinning is its main deformation mechanism. However, twinning is sometimes not applicable to the α-phase in dual-phase Ti alloys, as the presence of the β-phase could affect the plastic deformation mode of the α-phase [33]. The β-phase has more active slip systems than the α-phase, but the dislocation's slip direction is different from that of the neighboring α-phase, so the phase boundary has a strong locking effect on the moving dislocations, making subsequent plastic deformation increasingly difficult [30]. In order to coordinate plastic deformation, at least five independent slip systems are required for the same α- and β-phases according to the von Mises criterion [33]. For the α-phase, dislocations can easily slip on the prismatic plane $\{10\,\bar{1}0\}$ and along the $\langle\bar{1}120\rangle$ slip directions on the pyramidal plane (0002) under the uncoordinated plastic deformation conditions, apart from the $\{0001\}$ base plane [34]. Meanwhile, the slip systems that are more difficult to open may slide under conditions of SPD. Therefore, the uncoordinated plastic deformation drives the opening of more slip systems in the α-phase more easily than the activation of deformation twins, thus making the surface nanocrystallization mechanism of the TC11 alloy after SFPB mainly dominated by a dislocation motion.

During continuous bombardment by Al_2O_3 particles, the dislocations kept moving and rearranging under the stress. Because of the hindering effect of the α/β-phase boundary [35], a high density of dislocation tangles could form at the α/β-phase interface (Fig. 8(a)), which retarded plastic deformation and induced more slip systems in the α-phase. As the strain increased, dislocations proliferated greatly, and then aggregated into different dislocation structures (Figs. 8(d, f)). The dislocations were rearranged into dislocation walls with different thicknesses and orientations through slip, accumulation, interaction and possible annihilation, and ran through the whole α-lamellae, which eventually led to the splitting of the α-lamellae (Fig. 8(h)). At higher stresses, dislocation walls could also cross phase boundaries, causing the fragmentation of the α- and β-lamellae (Fig. 8(h)). As the stress increased further, dislocation walls and tangles also continued to be generated within the fragmented subgrains, splitting the grains into even smaller fragments. When the rates of dislocation generation and annihilation reached equilibrium, the subgrain boundaries gradually transformed into high-angle grain boundaries [1,22,31], leading to the formation of fine nanocrystals. When the strain continued to increase, there was no longer a continued reduction in grain size. At this time as the smaller grain size dislocation confinement was more serious, the energy within the grain was reduced, which led to the rotation of nanocrystals. So, the SFPB-treated TC11 alloy finally succeeded in obtaining randomly oriented nanocrystals.

During SFPB, Al_2O_3 bombarded the sample's surface at high speed, and the strain rate and deformation gradually decreased as the distance from the topmost surface increased. Therefore, the lamellae on the surface of the TC11 alloy were transformed into randomly oriented nanocrystals after SFPB, whereas the subsurface retained the lamellar morphology. The original orientation of the α- and β-lamellae was still preserved, but the

lamellar microstructure underwent bending, and dislocation increased with an increase in the SFPB gas pressure. In addition, the strain rate of the surface layer increased gradually with the increase of SFPB gas pressure. Nonetheless, when the SFPB gas pressure reached a certain value, the grain refinement and microstrain reached saturation. This is because when the size of a nanocrystal is reduced to a certain level, the nanocrystal is basically stable because the dislocation motion will be spatially restricted [36]. Continuous increase in the strain rate can only result in the rotation of the nanocrystal or migration of the grain boundaries.

3.3 Mechanical properties

3.3.1 Residual stress

Figure 9 displays the residual stress in different layer depths of the TC11 alloy after SFPB with different gas pressures. There was a small tensile stress in the TC11 alloy before SFPB, around 8 MPa, which may have been generated by machining. After SFPB, compressive residual stress (CRS) field at a certain depth was induced on the surface of the TC11 alloy under the combined effect of plastic deformation and volume limitation [37]. The depth of the CRS field increased with the increase of gas pressure, which was 160, 200 and 220 μm at 0.5, 1.0 and 1.5 MPa, respectively. In addition, it was found that similar to traditional shot peening, the maximum CRS was located on the subsurface, which is different from the experimental result that the maximum CRS was located on the surface after LSP [38]. The maximum CRS was located on the subsurface after SFPB because SFPB was used to directly impact the material surface with a large number of high-speed Al_2O_3 particles, which caused severe distortion of the grains. When the strain rate was too high, the projectile impact force could not be transferred to the surrounding material fast enough to cause an increase in energy, resulting in a rise in the surface temperature, which led to a dynamic recovery phenomenon, causing the surface CRS to relax and the maximum CRS to move to the subsurface. In contrast, LSP was a typical cold processing, with no contact with the material surface, no heat-affected zone, and better stability of the obtained residual stress, so the maximum CRS was located on the surface after LSP [39]. The location of the maximum CRS was farther away from the surface as the gas pressure increased, and it was usually located a few tens of microns (20−40 μm) from the surface. The maximum CRS of −452, −478, and −533 MPa was obtained at 0.5, 1.0 and 1.5 MPa, respectively. It could also be found that the surface CRS did not differ much and relax at 1.5 MPa, which was due to the plastic deformation of the surface gradually fully and saturated as the gas pressure increased and the CRS was released at the crack tip due to the formation of surface cracks at 1.5 MPa, leading to the decrease in the CRS.

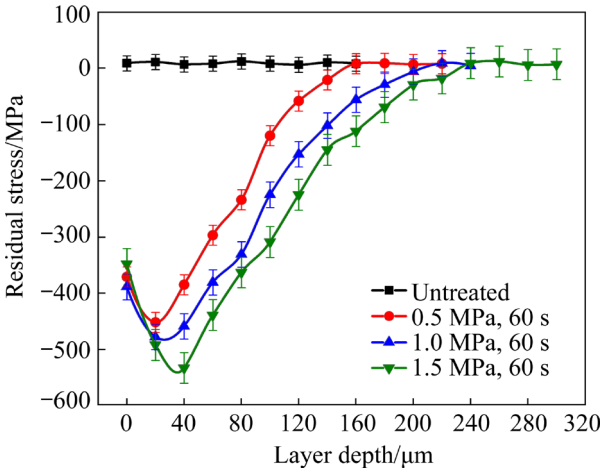

Fig. 9 Residual stress in different layer depths of TC11 alloy after SFPB with different gas pressures

3.3.2 Mechanical properties

The microhardness at different depths of the TC11 alloy after SFPB is given in Fig. 10. The microhardness of the TC11 alloy is about $HV_{0.1}$ 310 before SFPB, whereas the surface microhardness increases to $HV_{0.1}$ 357 (0.5 MPa), $HV_{0.1}$ 374 (1.0 MPa) and $HV_{0.1}$ 398 (1.5 MPa) after SFPB, corresponding to an increase of 15.2%, 20.6% and 28.4%, respectively. It can also be seen from Fig. 10 that with an increase in the distance from the surface, the microhardness decreases rapidly within distance from the surface of 0−40 μm, then shows a roughly linear decreasing trend, finally converging gradually to a stable value close to the matrix microhardness at depths of 100 μm (0.5 MPa), 160 μm (1.0 MPa) and 180 μm (1.5 MPa). This depth can be considered to be the thickness of the hardened layer after SFPB, suggesting that increasing the SFPB gas pressure has a significant role in enhancing the surface microhardness and the thickness of the hardened layer of the TC11 alloy.

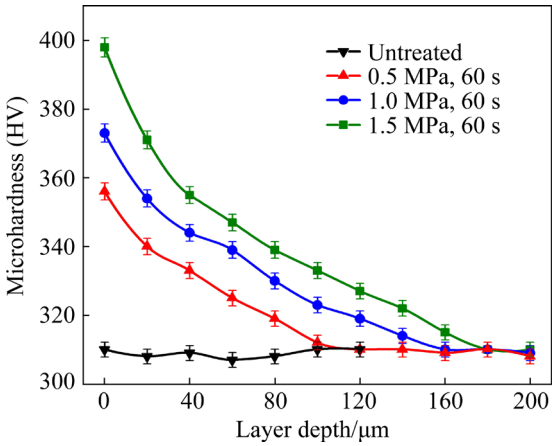

Fig. 10 Microhardness of TC11 alloy at different depths after SFPB with different gas pressures

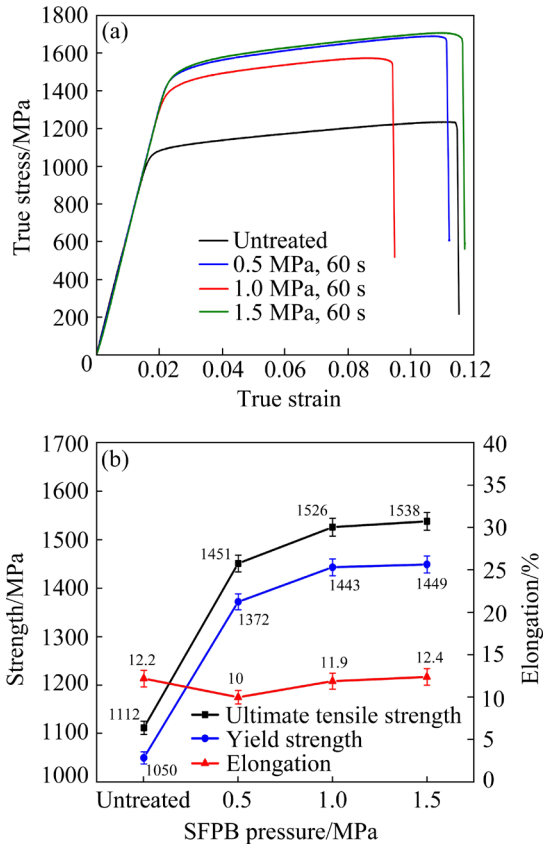

Fig. 11 Tensile mechanical properties of TC11 alloys after SFPB with different gas pressures: (a) True stress–strain curves; (b) Mechanical properties

These are two critical factors that lead to such a great increase in the surface microhardness, which increases with decreasing grain size and is positively correlated with dislocation density [40]. Firstly, the surface of the TC11 alloy undergoes high strain rate deformation during SFPB, which causes dislocations to be generated and to proliferate inside the grains. The formation of high-density dislocations increases the resistance to dislocation movement, thus inducing the work hardening phenomenon. Secondly, the surface nanocrystals increase the grain boundaries, thus enhancing the intergranular bonding. As the distance from the surface increases, the SFPB's impact kinetic energy gradually decreases, and the effects of grain refinement and work hardening gradually decrease (Fig. 5), resulting in a gradient decrease in the microhardness.

Representative true stress–strain curves and the corresponding mechanical properties obtained for the TC11 alloys are shown in Fig. 11. The yield and ultimate tensile strengths of the TC11 alloy after SFPB are improved significantly, consistent with the microhardness measurement, increased by 30.7%, 37.4%, 38% and 30.4%, 37.2%, 38.3% at SFPB gas pressures of 0.5, 1.0 and 1.5 MPa, respectively. It is noteworthy that the SFPB treatment does not noticeably affect the elongation.

The strength of the TC11 alloy after SFPB was evaluated according to Eq. (2) [41]:

$$\sigma_f=\sigma_0+kd_{fp}^{-1/2}+\alpha Gb\rho^{1/2} \quad (2)$$

where σ_f is the strength, σ_0 is the friction stress, k is the Hall−Petch constant, d_{fp} is the dislocation mean free path, α is a constant, G is the shear modulus, b is the amplitude of Burgers vector, and ρ is the dislocation density. In Eq. (2), the σ_f and d_{fp} are inversely proportional. Repeated bombardment of the TC11 alloy's surface by Al_2O_3 particles causes irreversible permanent microdents on the surface and the formation of a SPD layer underneath (Fig. 5). A gradient nanostructure, consisting of a surface layer with randomly oriented nanocrystals and a subsurface layer still possessing a lamellar microstructure, was obtained (Figs. 7 and 8). The effect of gradient nanostructures on the d_{fp} with increasing gas pressure is as follows: firstly, the increase in surface nanocrystallization with increasing SFPB gas pressure, makes d_{fp} decrease; secondly, with a decrease in the subsurface lamellar spacing, as well as an increase in the SPD layer with increasing SFPB gas pressure, the area of reduced lamellae spacing increases and the d_{fp} decreases accordingly. In short, with an increase in the gas pressure, the dislocation mean free path, d_{fp}, decreases, which produces a subsequent increase in

the yield and tensile strengths of the TC11 alloy.

The increase in strength after SFPB is also inextricably linked to the high CRS and microhardness obtained after SFPB. The presence of a CRS field can readjust the distribution of residual stresses in the components. It can offset part of the surface tensile stress formed during loading, thus shifting the maximum tensile stress to the subsurface layer. In turn, on the one hand, this leads to the formation of cracks on the subsurface. On the other hand, the CRS can prevent crack expansion and close the cracks, thus leading to the enhancement of the strength of the components [42]. Additionally, work hardening occurs after SFPB, which results in an increase in the local strength of the surface [43]. However, when the gas pressure increases to 1.5 MPa, cracks will form on the surface (Fig. 4(g)), making crack nucleation easier and causing the release of CRS. Thus, the improvement in strength is not significant at 1.5 MPa in comparison with that at 1.0 MPa.

The insignificantly influenced elongation may be related to the increase in uncoordinated plastic deformation on the subsurface with increasing gas pressure. It results in more slip systems being activated in the α-phase [44], leading to an uncompromised material plasticity, along with the enhanced strength.

3.3.3 Tensile fracture morphology

Figure 12 shows the tensile fracture morphology of the TC11 alloy subjected to diverse SFPB gas pressures. The tensile fracture has large and deep dimples and shows the typical ductile fracture characteristics before SFPB (Fig. 12(a)). After SFPB (Figs. 12(b−d)), the fracture morphology of the TC11 alloy shows a mixed fracture characteristic of quasi-cleavage and ductility. Unlike internal matrix fractures, fractures of the hardened surface contain a large number of cleavage surfaces and a small number of dimples. As the SFPB gas pressure increases, the proportion of dimples and the area of cleavage near the surface increase. This can be explained by the fact that the SPD layer is deeper at greater SFPB gas pressures (Fig. 5). Meanwhile, an increase in the SFPB gas pressure drives an increase in slip systems in the α-phase and therefore promotes plasticity, resulting in a larger proportion of dimples near the surface.

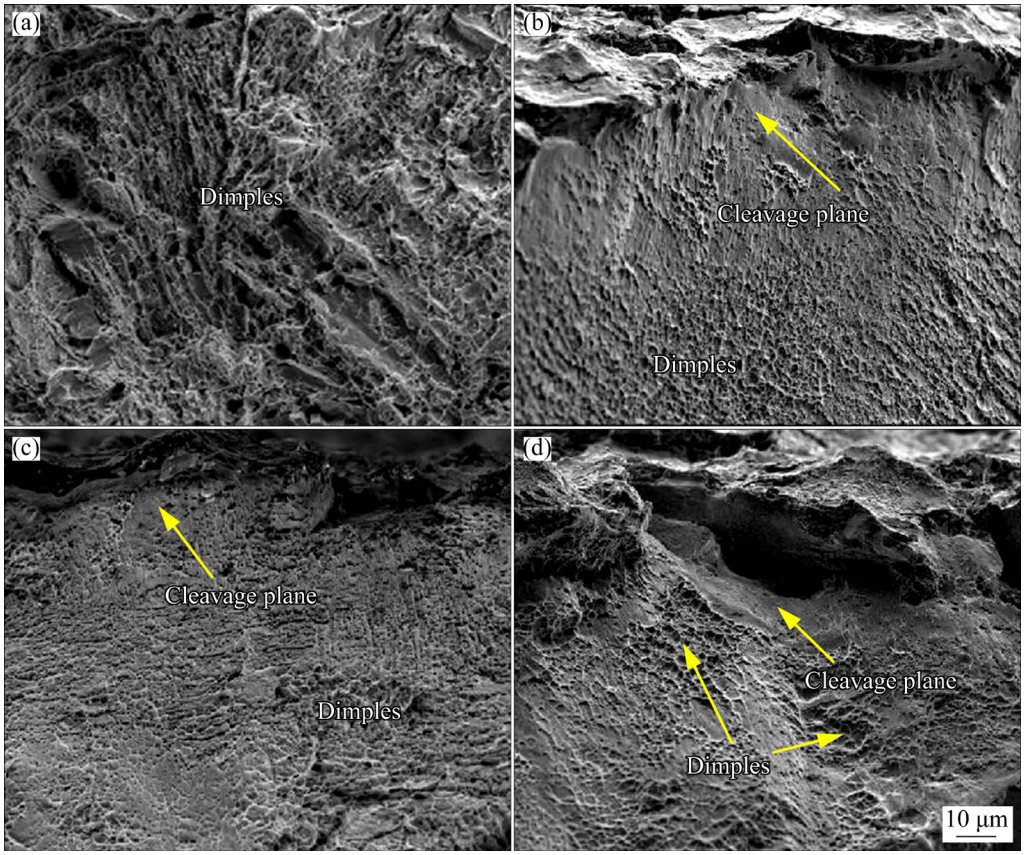

Fig. 12 Tensile fracture morphology of TC11 alloy after SFPB with different gas pressures: (a) Untreated; (b) 0.5 MPa for 60 s; (c) 1.0 MPa for 60 s; (d) 1.5 MPa for 60 s

4 Conclusions

(1) Gradient nanostructures were created on the TC11 alloy's surface by SFPB with different gas pressures (0.5, 1.0 and 1.5 MPa). The surface's lamellar microstructure was completely fragmented into nanometer-sized grains. The nanocrystal size decreased with increasing gas pressure, about 9.4 nm at 1.5 MPa, whereas the subsurface retained its initial lamellar microstructure and its dislocation density increased with increasing gas pressure.

(2) The surface roughness decreased and then increased with the increase of gas pressure, and the surface roughness was minimal at 1.0 MPa. Surface microcracks formed at 1.5 MPa, and thus the surface compressive residual stress decreased.

(3) The yield and ultimate tensile strengths increased significantly after SFPB although the elongation did not change much. The strength values at 1.5 MPa were not significantly different from those at 1.0 MPa. Thus, the best strength–plasticity match was achieved at 1.0 MPa, when the yield and ultimate tensile strengths reached 1443 and 1526 MPa, respectively, which were increased by 37.4% and 37.2%, respectively, compared with those without SFPB. The fracture morphology of the TC11 alloy changed from typical ductile fracture to quasi-cleavage and ductile mixed fracture after SFPB.

Acknowledgments

This work was supported by the National Natural Science Foundation of China (Nos. U1804146, 51801054, 52111530068), the Program for Science and Technology Innovation Talents in Universities of Henan Province, China (No. 17HASTIT026), the Foreign Experts Introduction Project of Henan Province, China (No. HNGD2020009), the Science and Technology Innovation Team of Henan University of Science and Technology, China (No. 2015XTD006), and the Academy of Finland (No. 311934).

References

[1] ZHANG Cheng-wei, FU Tian-lin, CHEN Han-yue, GAO Yan. Microstructure evolution of surface gradient nano-crystalline by shot peening of TA17 titanium alloy [J]. Metallurgical and Materials Transactions A, 2021, 52: 1790−1798.

[2] XU Jian-wei, ZENG Wei-dong, ZHOU Da-di, HE Sheng-tong, JIA Run-chen. Evolution of coordination between α and β phases for two-phase titanium alloy during hot working [J]. Transactions of Nonferrous Metals Society of China, 2021, 31(11): 3428−3438.

[3] ELSHAER R N, IBRAHIM K M. Effect of cold deformation and heat treatment on microstructure and mechanical properties of TC21 Ti alloy [J]. Transactions of Nonferrous Metals Society of China, 2020, 30(5): 1290−1299.

[4] LIU Y G, LI H M, LI M Q. Roles for shot dimension, air pressure and duration in the fabrication of nanocrystalline surface layer in TC17 alloy via high energy shot peening [J]. Journal of Manufacturing Processes, 2020, 56: 562−570.

[5] DAI Shi-juan, ZHU Yun-tian, HUANG Zhao-wen. Microstructure evolution and strengthening mechanisms of pure titanium with nano-structured surface obtained by high energy shot peening [J]. Vacuum, 2016, 125: 215−221.

[6] KUMAR S A, RAMAN S S, SANKARA NARAYANAN T S N. Influence of surface mechanical attrition treatment duration on fatigue lives of Ti−6Al−4V [J]. Transactions of the Indian Institute of Metals, 2014, 67(1): 137−141.

[7] YANG Zhen-wen, LIU Qi, WANG Jia-hui, MA Zong-qing, WANG Ying, WANG Dong-po. Effect of ultrasonic impact treatment on the microstructure and mechanical properties of diffusion-bonded TC11 alloy joints [J]. Archives of Civil and Mechanical Engineering, 2019, 19(4): 1431−1441.

[8] KUMAR P, MAHOBIA G S, CHATTOPADHYAY K. Surface nanocrystallization of β-titanium alloy by ultrasonic shot peening [J]. Materials Today: Proceedings, 2020, 28: 486−490.

[9] NIE Xiang-fan, HE Wei-feng, CAO Zhen-yang, SONG Jing-dong, LI Xiang, PANG Zhi-cong, YAN Xue-yuan. Experimental study and fatigue life prediction on high cycle fatigue performance of laser-peened TC4 titanium alloy [J]. Materials Science and Engineering A, 2021, 822: 141658.

[10] PIERRE M, LAYRENT W, PHILIPPE B, THIERRY G. Effects of SMAT at cryogenic and room temperatures on the kink band and martensite formations with associated fatigue resistance in a β-metastable titanium alloy [J]. Materials Science and Engineering A, 2021, 803: 140618.

[11] ZHANG Qi, DUAN Bing-bing, ZHANG Zi-qian, WANG Jun-biao, SI Chao-run. Effect of ultrasonic shot peening on microstructure evolution and corrosion resistance of selective laser melted Ti−6Al−4V alloy [J]. Journal of Materials Research and Technology, 2021, 11: 1090−1099.

[12] KONG Ling-yan, LAO Yuan-xia, XIONG Tian-ying, LI Tie-fan. Nanocrystalline surface layer on AISI 52100 steel induced by supersonic fine particles bombarding [J]. Journal of Thermal Spray Technology, 2013, 22(6): 1007−1013.

[13] ZHANG Liu-yan, MA Ai-bin, JIANG Jing-hua, SONG Dan, YANG Dong-hui, CHEN Jian-qing. Electrochemical corrosion properties of the surface layer produced by supersonic fine-particles bombarding on low-carbon steel [J]. Surface and Coatings Technology, 2013, 232: 412−418.

[14] ZHOU Tian, XIONG Yi, CHEN Zheng-ge, ZHA Xiao-qin, LU Yan, HE Tian-tian, REN Feng-zhang, SINGH H, KÖMI J, HUTTULA M, CAO Wei. Effect of surface nano-crystallization induced by supersonic fine particles bombarding on microstructure and mechanical properties of

300M steel [J]. Surface and Coatings Technology, 2021, 421: 127381.

[15] LIU Ke-jing, CUI Xiu-fang, DONG Mei-ling, XING Zhi-guo, LI Jian, TIAN Hao-liang, JIN Guo, WANG Hai-dou, XU Bin-shi. Mechanism of diffusion promotion of carbon atoms during carburization of 20Cr2Ni4A alloy steel after lanthana-bearing supersonic fine particle bombarding pretreatment [J]. Surface and Coatings Technology, 2021, 425: 127702.

[16] GAO Hong-mei, CHEN Wen-ge, ZHANG Zhi-jun. Evolution mechanism of surface nano-crystallization of tungsten−copper alloys [J]. Materials Letters, 2016, 176: 181−184.

[17] ZHANG Yu-xiang, YANG Jian-hai, GE Li-ling, ZHANG Xin, CHEN Jia-zhao. Research on mechanism of surface nanocrystalline layer in 2219 Al alloy induced by supersonic fine particles bombarding [J]. International Journal of Engineering Research in Africa, 2016, 4438(24): 1−8.

[18] ZHANG Bao-sen, DONG Qiang-sheng, BA Zhi-xin, WANG Zhang-zhong, SHI Han-cheng, XUE Yan-ting. Tribological properties of surface-textured and plasma-nitrided pure titanium under oil lubrication condition [J]. Journal of Materials Engineering and Performance, 2018, 27: 186−193.

[19] GE Li-ling, YUAN Zhan-wei, JING Xiao-tian, LU Zheng-xin. Study of pure titanium (TA2) surface nanocrystallization and its thermal stablity [J]. Rare Metal and Engineering, 2011, 40(7): 1239−1242. (in Chinese)

[20] GE Li-ling, YUAN Zhan-wei, HAN Zhen-hua. Creep behavior of commercially pure titanium TA2 after supersonic fine particles bombardment [J]. Journal of Materials Engineering and Performance, 2019, 28(2): 1141−1150.

[21] ZHAO Kun, WANG Min, LIN Cheng-xiao, TUO Chuan. Mechanism and nanostructure evolution of surface self-nanocrystallization of TC17 [J]. Rare Metal and Engineering, 2013, 42(10): 2048−2052. (in Chinese)

[22] WU Yong-li, XIONG Yi, LIU Wei, CHEN Zheng-ge, ZHANG Xin, WANG Shu-bo, CAO Wei. Effect of supersonic fine particle bombardment on microstructure and fatigue properties of Ti−6.5Al−3.5Mo−1.5Zr−0.3Si titanium alloy at different temperatures [J]. Surface and Coatings Technology, 2021, 421: 127473.

[23] ZHANG Cong-hui, HU Kun, ZHENG Min, ZHU Wen-guang, SONG Guo-dong. Effect of surface nanocrystallization on fatigue properties of Ti−6Al−4V alloys with bimodal and lamellar structure [J]. Materials Science and Engineering A, 2021, 813: 141142.

[24] LIU Y G, LI M Q, LIU H J. Nanostructure and surface roughness in the processed surface layer of Ti−6Al−4V via shot peening [J]. Materials Characterization, 2017, 123: 83−90.

[25] TRUNG P Q, KHUN N W, BUTLER D L. Effects of shot peening pressure, media type and double shot peening on the microstructure, mechanical and tribological properties of low-alloy steel [J]. Surface Topography: Metrology and Properties, 2016, 4(4): 045001.

[26] YANG C, LIU Y G, LI M Q. Characteristics and formation mechanisms of defects in surface layer of TC17 subjected to high energy shot peening [J]. Applied Surface Science, 2020, 509: 144711.

[27] ZOU Shi-kun, WU Jun-feng, ZHANG Yong-kang, GONG Shui-li, SUN Gui-fang, NI Zhong-hua, CAO Zi-wen, CHE Zhi-gang, FENG Ai-xin. Surface integrity and fatigue lives of Ti17 compressor blades subjected to laser shock peening with square spots [J]. Surface and Coatings Technology, 2018, 347: 398−406.

[28] UNAL O, MALEKI E, VAROL R. Effect of severe shot peening and ultra-low temperature plasma nitriding on Ti−6Al−4V alloy [J]. Vacuum, 2018, 150: 69−78.

[29] YANG C, LI M Q, LIU Y G. Further refinement mechanisms of nanograins in nanocrystalline surface layer of TC17 subjected to severe plastic deformation [J]. Applied Surface Science, 2021, 538: 147941.

[30] LI Xin, DENG Si-ying, WANG Song-wei, SONG Hong-wu, ZHANG Shi-hong, WANG Ke-lu, OUYANG De-lai. Dynamic globularization mechanism during hot working of Ti−6.5Al−3.5Mo−1.5Zr−0.3Si alloy with lamellar microstructure [J]. Materials Characterization, 2021 171: 110749.

[31] NIE Xiang-fan, HE Wei-feng, ZANG Shun-lai, WANG Xue-de, ZHANG Jie. Effect study and application to improve high cycle fatigue resistance of TC11 titanium alloy by laser shock peening with multiple impacts [J]. Surface and Coatings Technology, 2014, 253: 68−75.

[32] LUO Si-hai, ZHOU Liu-cheng, WANG Xue-de, CAO Xin, NIE Xiang-fan, HE Wei-feng. Surface nanocrystallization and amorphization of dual-phase TC11 titanium alloys under laser induced ultrahigh strain-rate plastic deformation [J]. Materials, 2018, 11(4): 563.

[33] LI Chuang, CUI Wen-fang, ZHANG Yu-sheng. Surface self-nanocrystallization of α+β titanium alloy by surface mechanical grinding treatment [J]. Metals and Materials International, 2017, 23(3): 512−518.

[34] AO Ni, LIU Dao-xin, XU Xing-chen, ZHANG Xiao-hua, LIU Dan. Gradient nanostructure evolution and phase transformation of α phase in Ti−6Al−4V alloy induced by ultrasonic surface rolling process [J]. Materials Science and Engineering A, 2019, 742: 820−834.

[35] SUN Hong, YU Li-ming, LIU Yong-chang, ZHANG Li-ye, LIU Chen-xi, LI Hui-jun, WU Jie-feng. Effect of heat treatment processing on microstructure and tensile properties of Ti−6Al−4V−10Nb alloy [J]. Transactions of Nonferrous Metals Society of China, 2019, 29(1): 59−66.

[36] ZHOU X, LI X Y, LU K. Enhanced thermal stability of nanograined metals below acritical grain size [J]. Science, 2018, 360: 526−530.

[37] YIN Mei-gui, CAI Zhen-bing, LI Zhen-yang, ZHOU Zhong-rong, WANG Wen-jian, HE Wei-feng. Improving impact wear resistance of Ti−6Al−4V alloy treated by laser shock peening [J]. Transactions of Nonferrous Metals Society of China, 2019, 29(7): 1439−1448.

[38] XIONG Yi, HE Tian-tian, LI Peng-yan, CHEN Lu-fei, REN Feng-zhang, VOLINSKY A A. Effects of laser pulse energy on surface microstructure and mechanical properties of high carbon steel [J]. Journal of Central South University, 2015, 22(12): 4515−4520 .

[39] MA Yun-fei, XIONG Yi, CHEN Zheng-ge, ZHA Xiao-qin, HE Tian-tian, LI Yong, SINGH H, KÖMI J, HUTTULA M,

CAO Wei. Microstructure evolution and properties of gradient nanostructures subjected to laser shock processing in 300M ultrahigh-strength steel [J]. Steel Research International, 2022, 93(2): 2100434.

[40] LIU Hua-bing, WEI Xiao-xiao, XING Shi-long, WANG Lian-bo, ZHU Wen-long, JIANG Chuan-hai, VINCENT J, ZHAN Ke. Effect of stress shot peening on the residual stress field and microstructure of nanostructured Mg−8Gd−3Y alloy [J]. Journal of Materials Research and Technology, 2021, 10: 74−83.

[41] LIU Dan, LIU Dao-xin, ZHANG Xiao-hua, LIU Cheng-song, AO Ni. Surface nanocrystallization of 17-4 precipitation-hardening stainless steel subjected to ultrasonic surface rolling process [J]. Materials Science and Engineering A, 2018, 726: 69−81.

[42] LUO Xian, REN Xue-ping, JIN Qi, QU Hai-tao, HOU Hong-liang. Microstructural evolution and surface integrity of ultrasonic surface rolling in Ti_6Al_4V alloy [J]. Journal of Materials Research and Technology, 2021, 13: 1586−1598.

[43] LIU Hua-bing, ZHU Wen-long, JIANG Chuan-hai, MARIO G L, XING Shi-long, WANG Lian-bo, VINCENT J, ZHAN Ke. Microstructure evolution and residual stress distribution of nanostructured Mg−8Gd−3Y alloy induced by severe shot peening [J]. Surface and Coatings Technology, 2020, 404: 126465.

[44] ZHANG He-peng, CAI Zhong-yi, WAN Zhan-dong, PENG Peng, ZHANG Hong-qiang, SUN Ru-jian, CHE Zhi-gang, GUO Chao, LI Bo, GUO Wei. Microstructure and mechanical properties of laser shock peened 38CrSi steel [J]. Materials Science and Engineering A, 2020, 788: 139486.

超音速微粒轰击气体压力对 TC11 钛合金显微组织和力学性能的影响

武永丽[1]，熊 毅[1,2]，陈正阁[3]，刘 伟[1,2]，张 鑫[1]，王树泊[4]，曹 伟[4]

1. 河南科技大学 材料科学与工程学院，洛阳 471023；
2. 有色金属新材料与先进加工技术省部共建协同创新中心，洛阳 471023；
3. 西北核技术研究所 激光与物质相互作用国家重点实验室，西安 710024；
4. Nano and Molecular Systems Research Unit, University of Oulu, FIN-90014, Finland

摘 要：借助超音速微粒轰击(SFPB)对片层组织的 Ti−6.5Al−3.5Mo−1.5Zr−0.3Si (TC11) 钛合金进行表面纳米化处理，并系统研究 SFPB 气体压力对其表面完整性、显微组织演变和力学性能的影响规律。结果表明，在不同 SFPB 气体压力下，TC11 钛合金表层均已形成梯度纳米结构。表层片层组织晶粒尺寸完全碎化至纳米量级，且纳米晶晶粒尺寸随着气体压力的增大而减小，而次表层组织仍保留原始片层形貌。经 1.0 MPa 处理后，表面粗糙度最小，在 1.5 MPa 时表面形成微裂纹，表层残余压应力下降。随着 SFPB 气体压力的增大，表层显微硬度及硬化层深度逐渐增加，屈服强度、抗拉强度增加，而伸长率变化不大，断口形貌从典型的韧性断裂向准解理和韧性混合型断裂转变。

关键词：超音速微粒轰击；气体压力；钛合金；片层组织；表面纳米化；显微组织；力学性能

(Edited by Wei-ping CHEN)